Energy-dispersive X-ray emission spectroscopy using an X-ray free-electron laser in a shot-by-shot mode

Roberto Alonso-Mori[a], Jan Kern[a,b], Richard J. Gildea[b], Dimosthenis Sokaras[c], Tsu-Chien Weng[c], Benedikt Lassalle-Kaiser[b], Rosalie Tran[b], Johan Hattne[b], Hartawan Laksmono[d], Julia Hellmich[e], Carina Glöckner[e], Nathaniel Echols[b], Raymond G. Sierra[d], Donald W. Schafer[a], Jonas Sellberg[c,f], Christopher Kenney[a,c], Ryan Herbst[a,c], Jack Pines[a,c], Philip Hart[a,c], Sven Herrmann[a,c], Ralf W. Grosse-Kunstleve[b], Matthew J. Latimer[c], Alan R. Fry[a], Marc M. Messerschmidt[a], Alan Miahnahri[a], M. Marvin Seibert[a], Petrus H. Zwart[b], William E. White[a], Paul D. Adams[b], Michael J. Bogan[a,e], Sébastien Boutet[a], Garth J. Williams[a], Athina Zouni[e], Johannes Messinger[g], Pieter Glatzel[h], Nicholas K. Sauter[b], Vittal K. Yachandra[b,1], Junko Yano[b,1], and Uwe Bergmann[a,1]

[a]Linac Coherent Light Source, SLAC National Accelerator Laboratory, Menlo Park, CA 94025; [b]Physical Biosciences Division, Lawrence Berkeley National Laboratory, Berkeley, CA 94720; [c]Stanford Synchrotron Radiation Lightsource, SLAC National Accelerator Laboratory, Menlo Park, CA 94025; [d]PULSE Institute, SLAC National Accelerator Laboratory, Menlo Park, CA 94025; [e]Max-Volmer-Laboratorium für Biophysikalische Chemie, Technische Universität, D-10623 Berlin, Germany; [f]Department of Physics, AlbaNova, Stockholm University, S-106 91 Stockholm, Sweden; [g]Institutionen för Kemi, Kemiskt Biologiskt Centrum, Umeå Universitet, Umeå, Sweden; and [h]European Synchrotron Radiation Facility, F-38043 Grenoble Cedex, France

Edited by Harry B. Gray, California Institute of Technology, Pasadena, CA, and approved October 16, 2012 (received for review July 7, 2012)

The ultrabright femtosecond X-ray pulses provided by X-ray free-electron lasers open capabilities for studying the structure and dynamics of a wide variety of systems beyond what is possible with synchrotron sources. Recently, this "probe-before-destroy" approach has been demonstrated for atomic structure determination by serial X-ray diffraction of microcrystals. There has been the question whether a similar approach can be extended to probe the local electronic structure by X-ray spectroscopy. To address this, we have carried out femtosecond X-ray emission spectroscopy (XES) at the Linac Coherent Light Source using redox-active Mn complexes. XES probes the charge and spin states as well as the ligand environment, critical for understanding the functional role of redox-active metal sites. $K\beta_{1,3}$ XES spectra of Mn^{II} and $Mn_2^{III,IV}$ complexes at room temperature were collected using a wavelength dispersive spectrometer and femtosecond X-ray pulses with an individual dose of up to >100 MGy. The spectra were found in agreement with undamaged spectra collected at low dose using synchrotron radiation. Our results demonstrate that the intact electronic structure of redox active transition metal compounds in different oxidation states can be characterized with this shot-by-shot method. This opens the door for studying the chemical dynamics of metal catalytic sites by following reactions under functional conditions. The technique can be combined with X-ray diffraction to simultaneously obtain the geometric structure of the overall protein and the local chemistry of active metal sites and is expected to prove valuable for understanding the mechanism of important metalloproteins, such as photosystem II.

energy-dispersive XES | Kβ emission lines | femtosecond x-ray spectroscopy

The first X-ray free-electron laser (XFEL) operating in the hard X-ray regime (1), the Linac Coherent Light Source (LCLS), produces ~5- to 400-fs X-ray pulses with up to $\sim 10^{12}$ photons per pulse at 6–10 keV at a repetition rate of 120 Hz. Each of these X-ray pulses is intense enough to expel multiple electrons from the target, which can lead to a Coulomb explosion that destroys the sample. In a shot-by-shot experiment, data are collected from each pulse before the destruction of the sample, and the sample is replenished after each pulse. The feasibility of this "probe-before-destroy" approach for X-ray crystallography experiments using XFEL pulses was first demonstrated by Chapman et al. with various systems and has subsequently been corroborated by others at the LCLS (2–6).

Whereas X-ray crystallography is an important method for studying the geometric structure of entire complexes, X-ray absorption and emission spectroscopy are powerful techniques for studying the local chemistry in both inorganic systems and metalloproteins. X-ray absorption spectroscopy (XAS), where the unoccupied states are probed, has long been applied to various systems using synchrotron radiation (SR) (7–9), and recent advances in this methodology have made it possible to conduct time-resolved experiments in the picosecond domain (10–13). In recent years, X-ray emission spectroscopy (XES) has also been increasingly used at SR sources for the study of metalloproteins (14–16), geochemical systems (17–19), coordination complexes (20, 21), and inorganic catalytic centers (22). Complementary to XAS, XES probes the occupied electron levels and provides information about the electronic structure, charge/spin densities, and the nature of ligands (23–25). The $K\beta_{1,3}$ and $K\beta'$ lines probe the number of unpaired 3d electrons, hence providing information about the oxidation and/or spin state (14, 23). The $K\beta_{2,5}$ and $K\beta''$ lines result from ligand 2s/2p to metal 1s cross-over transitions and provide information about the ligand environment and symmetry (15, 16).

In contrast to XAS, the XES method requires a custom-built, high-resolution analyzer instrumentation capable of capturing a large solid angle of the emitted photons, which is not standard equipment at most X-ray sources (26, 27), and hence the method is not as commonly used as XAS techniques. However, XES has some important advantages that make it specifically suitable for XFEL applications: (*i*) the energy of the incident X-rays does not need to be varied to obtain an XES spectrum, and (*ii*) the incident X-ray energy and bandwidth is not critical as long as it is above the absorption edge of the element under study. Hence, XES can be adapted to shot-by-shot data collection when using energy-dispersive XES analyzer optics (28) to study the chemical intermediates and the time evolution of the reaction at room temperature (RT).

Chemical intermediate states, particularly in biological systems, have traditionally been studied by cryo-trapped methods at SR sources to understand the catalytic pathways (14). However, this approach does not allow real-time observation of the

Author contributions: R.A.-M., J.K., V.K.Y., J.Y., and U.B. designed research; R.A.-M., J.K., D.S., T.-C.W., B.L.-K., R.T., J. Hattne, H.L., J. Hellmich, C.G., N.E., R.G.S., D.W.S., J.S., A.R.F., M.M.M., M.M.S., M.J.B., S.B., G.J.W., A.Z., J.M., P.G., N.K.S., V.K.Y., J.Y., and U.B. performed research; J.K., R.J.G., J. Hattne, J. Hellmich, C.G., N.E., C.K., R.H., J.P., P.H., S.H., M.J.L., A.M., W.E.W., P.D.A., M.J.B., A.Z., N.K.S., V.K.Y., and J.Y. contributed new reagents/analytic tools; R.A.-M., J.K., R.J.G., J. Hattne, N.E., R.W.G.-K., P.H.Z., and N.K.S. analyzed data; and R.A.-M., J.K., D.S., J.M., V.K.Y., J.Y., and U.B. wrote the paper.

The authors declare no conflict of interest.

This article is a PNAS Direct Submission.

[1]To whom correspondence may be addressed. E-mail: bergmann@slac.stanford.edu, vkyachandra@lbl.gov, or JYano@lbl.gov.

electronic structural changes and/or bond forming/breaking at the wide range of time scales in which they are expected to occur. Major hurdles for conducting the experiments under ambient/functional conditions are the severe radiation damage at RT and the difficulty of acquiring time-resolved data with the required signal-to-noise ratio in a reasonable amount of time and with limited quantities of samples. This is in particular the case for most biological and biomimetic systems that work in dilute, aqueous environments. Therefore, at SR sources, X-ray absorption and emission spectra of most redox active biological/aqueous systems are collected under cryogenic conditions, thus minimizing diffusion of hydroxyl and other radical species that are the major cause of radiation damage (29–32).

XFEL-based spectroscopy has the potential for overcoming these limitations. Whereas time-dependent SR-based studies are generally limited to the picosecond time resolution of the source (13), X-ray spectroscopy at XFELs can be used to study the dynamics of the electronic structure in the femtosecond time domain. The ultrashort femtosecond X-ray pulses of XFELs can also overcome radiation damage caused by radical diffusion with the "probe-before-destroy" approach, because the time scale for radical diffusion is in the picosecond range. Moreover, the high flux of XFEL pulses should allow for the collection of time-resolved data from dilute samples or weak emission signals within a reasonable amount of time.

The feasibility of performing X-ray spectroscopy studies at XFELs has been questioned because of concerns regarding damage to the samples and other processes that may alter the intensities or spectral shapes caused by the intense X-ray pulses. In this work, we report the results of Mn $K\beta_{1,3}$ XES collected at room temperature in a shot-by-shot mode at the LCLS. The study determines the feasibility of XES using XFEL pulses and provides the basis for using XES to monitor the electronic state and integrity of the sample at XFELs.

Results and Discussion

X-Ray Damage. Two possible causes for X-ray–induced changes can be considered: (a) effects induced by sequential photon absorption within the time scale of the XFEL pulse and (b) Coulomb explosion caused by the accumulation of excessive charge in the molecule induced by the XFEL pulse. As discussed above, diffusion of X-ray–generated radicals, which destroy the integrity of the system, is not an issue in XFEL measurements.

First, XFEL pulses have been shown to create nonlinear effects at very high peak power densities, which could affect spectral features (33–39) and could be reflected as new spectral features at different energies (40). The probability for sequential ionizations is directly related to the product of the fluence and the photoionization cross-section. Considering the cross-section of the most probable 1s photoionization channel of Mn at 9.5 keV (1.4×10^{-4} Å^2/atom) and the maximum fluence used in this experiment ($\sim 2 \times 10^3$ photons/Å^2 per pulse, a flux of $\sim 1 \times 10^{12}$ photons per pulse focused to ~2 μm FWHM diameter at the sample position, corresponding to 500 MGy), the number of photons per Mn atom per pulse is ~0.1. If we include the lifetime of the Mn 1s core-hole (0.57 fs) with respect to the pulse length of ~50 fs, the probability for sequential ionization is estimated to be very low.

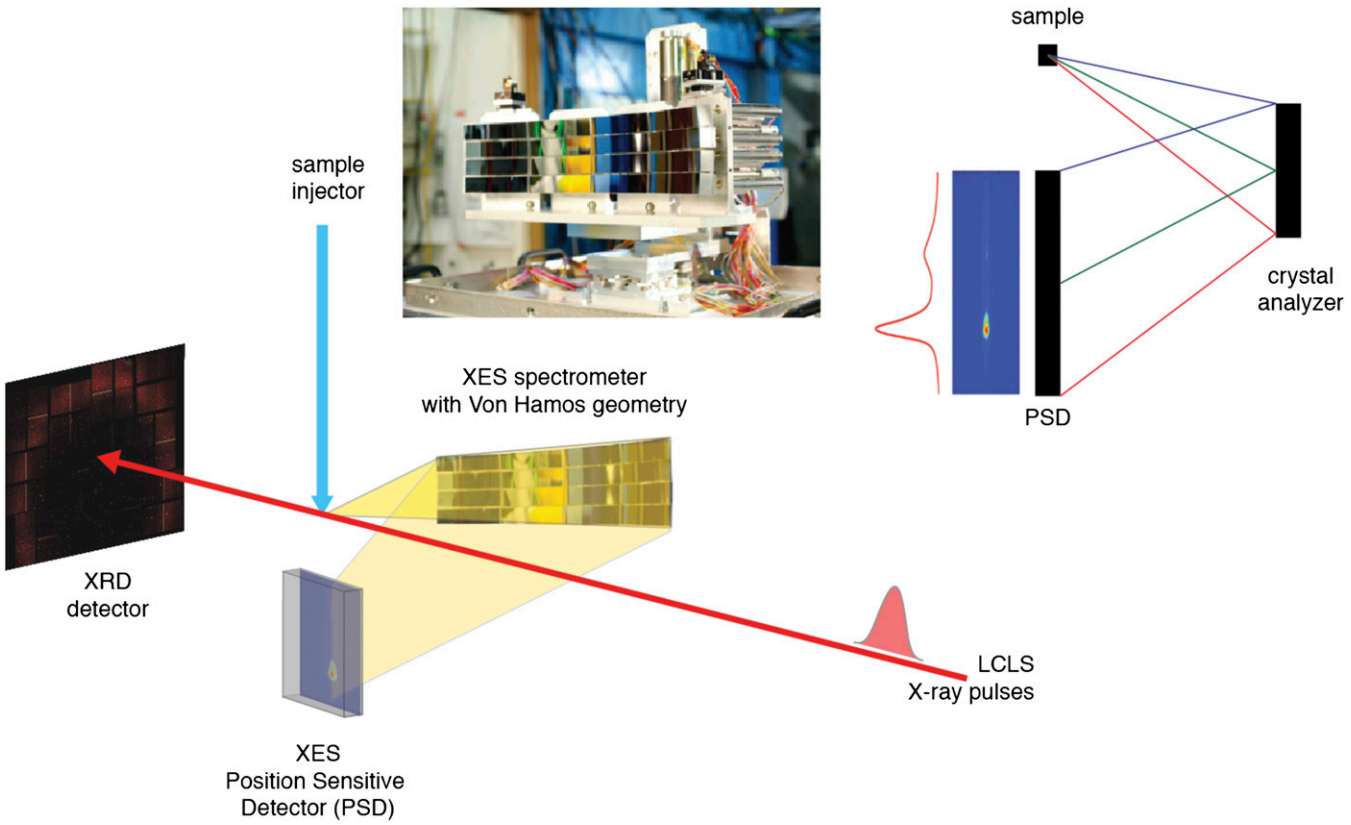

Fig. 1. (*Lower*) The energy-dispersive XES experimental setup. The setup allows simultaneous detection of X-ray diffraction (XRD) and X-ray emission spectra (XES) from a stream of crystals that intersects the XFEL beam. The XRD detector is downstream of the X-ray laser beam. The XES spectrometer is at 90° to the direction of the X-ray beam, focusing the emission spectrum on a custom-built 2D detector placed below the intersection point. (*Upper Right*) Vertical cut of the von Hamos geometry with a crystal analyzer and a position-sensitive detector; Bragg scattering from a point source is analyzed by the spectrometer array, resulting in an energy-dispersed spectrum on the detector. (*Upper Left*) A picture of the von Hamos spectrometer used in this work showing the array of 16 crystal analyzers.

Regarding the second point, the exact extent and time scale of the XFEL pulse-induced Coulomb explosion is not well understood and may depend on various parameters. For example, for hard X-ray pulses with a fluence of ~10^6 photons/Å^2 per pulse at 12.5 keV, the Coulomb explosion was calculated to occur in the tens of femtoseconds (41). It has also been shown, using X-ray diffraction (XRD) at 9.4 keV incident energy and a fluence of 3×10^2 photons/Å^2 per pulse, similar to that used in this study, that the damage in the geometric structure caused by the Coulomb explosion occurs on a time scale that is slow enough that a diffraction pattern can be obtained (6). XRD might even be self-terminating when the XFEL pulses are longer than the time required for causing damage (42). However, the situation is different for XES measurements, where electronic structural changes are probed. First, X-ray–induced electronic changes might already occur within the time scale of the XFEL pulse and without observable structural changes, and second, there is no self-termination by structural disorder in X-ray spectroscopy. The electronic rearrangements associated with a Coulomb explosion will also change the Mn oxidation state and hence will be reflected in the peak position and shape of the $K\beta_{1,3}$ line. This could lead to a misinterpretation of the spectra in terms of peak shifts. Hence, the feasibility of XES studies of redox active transition metal compounds at XFELs needs to be investigated before the technique can be more generally applied.

Energy-Dispersive X-Ray Emission Spectra. To address the above questions, $K\beta_{1,3}$ XES spectra were measured at the coherent X-ray imaging (CXI) instrument of the LCLS (43) using X-ray pulses of ~50 fs and ~100 fs pulse length at 7 keV and 9.5 keV. The samples were injected into the LCLS X-ray beam in a liquid jet (44). The spectra were collected in a shot-by-shot mode by means of a multicrystal energy-dispersive spectrometer (28) based on the von Hamos geometry (Fig. 1). The spectrometer consists of an array of 16 cylindrically bent crystal analyzers (500-mm radius) that diffract and focus the emitted signal onto a position-sensitive detector (*Materials and Methods*). The 2D spectra were recorded using a Cornell-SLAC Pixel Array Detector module composed of four 185- × 194-pixel CMOS ASICs (pixel size is 110×110 μm^2) bump-bonded to high-resistivity silicon diodes (45).

Two inorganic Mn complexes, $Mn^{II}Cl_2$ and $Mn_2^{III,IV}$Terpy (46) (*Materials and Methods*), were chosen as representative complexes for catalytically/functionally relevant oxidation states. Mn is an essential element in many inorganic and biological catalytic systems, such as the binuclear Mn active site in Mn catalase that disproportionates peroxide to O_2 and H_2O, and the Mn_4O_5Ca cluster in photosystem II that is responsible for photosynthetic water oxidation. Such redox active clusters are known to be prone to X-ray damage even at cryogenic temperatures (29), with higher-valent Mn species being reduced to Mn^{II}. $Mn_2^{III,IV}$Terpy contains bridging oxygen atoms between the Mn atoms, a motif that is known to be present in the active sites of both Mn catalase and photosystem II. Moreover, polynuclear synthetic manganese complexes bearing such μ-oxo bridges are also known for being active in oxidation catalysis and bleaching at industrial scales. $Mn^{II}Cl_2$ is a model for the oxidation state that is generated by X-ray damage at the inorganic/biological catalytic sites.

Fig. 2 shows the detector images of the $K\beta_{1,3}$ spectra of $Mn^{II}Cl_2$ (Fig. 2 *Left*) and $Mn_2^{III,IV}$Terpy (Fig. 2 *Right*) collected with 50-fs X-ray pulses at 9.5 keV. The $K\beta_{1,3}$ spectra originate

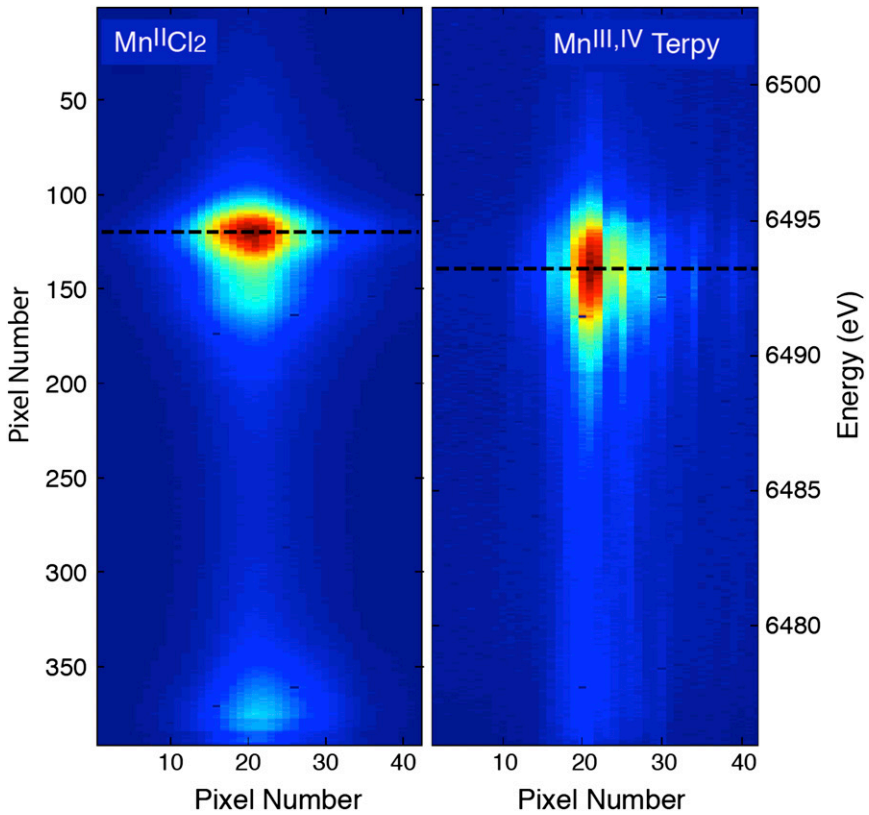

Fig. 2. The focused $K\beta_{1,3}$ XES spectra from all of the crystal analyzers. Two-dimensional images showing the Mn $K\beta_{1,3}$ X-ray emission spectra of (*Left*) $Mn^{II}Cl_2$ and (*Right*) $Mn_2^{III,IV}$Terpy collected at the LCLS. The images show the clear differences in the emission spectrum between the Mn^{II} and the $Mn_2^{III,IV}$ complexes. The vertical axis reflects the energy dispersion. Each of the crystals is tuned to focus the spectrum on the horizontal axis such that all 16 spectra coincide, thereby improving the signal-to-noise ratio.

from Mn 3p to 1s transitions and are sensitive indicators of the spin state of metal atoms through the 3p–3d exchange coupling. For high-spin Mn complexes, this translates into information about the oxidation state of the metal. The images are the average of ~100,000 individual shots (~13 min of data collection at a 120-Hz repetition rate of the LCLS). A count rate of ~1,000 counts per pulse in the whole spectral area was obtained for the $K\beta_{1,3}$ emission line from the $MnCl_2$ solution (500 mM Mn) in the few-micrometers-thick liquid jet, and thus sufficient statistics can be obtained after several seconds of data collection at the LCLS. The von Hamos geometry produces a linear dispersion of the XES energy in the vertical direction. The images show a shift in the position of the maximum intensity by ~18 pixels, which corresponds to an energy shift of 1.4 eV between the two compounds.

The Mn $K\beta_{1,3}$ emission lines are obtained by integrating the detector signal in the nondispersive horizontal direction (Fig. 3). The $K\beta_{1,3}$ peak positions of the $Mn^{II}Cl_2$ and $Mn_2^{III,IV}$Terpy are at 6,493.3 and 6,491.9 eV, respectively. The energy difference reflects the different number of unpaired 3d electrons in the two high-spin compounds (23). Fig. 3 also shows the spectra from $Mn^{II}Cl_2$ and $Mn_2^{III,IV}$Terpy solutions collected using synchrotron radiation. The Mn^{II} compound is not prone to photoreduction and was therefore collected at RT. In contrast, the $Mn^{III,IV}$ compound is readily reduced to Mn^{II} by diffusion of radicals, and therefore the synchrotron measurement of $Mn_2^{III,IV}$Terpy was conducted at cryogenic temperature (10 K) with low dose to avoid photoreduction. The LCLS and the synchrotron-based spectra for both compounds are in good agreement in the overall spectral shape and have the same energy shifts to within 0.05 eV (based on the pseudo-Voigt curve fits). This agreement shows that, under our experimental conditions, we can collect RT XES spectra at XFELs before the X-ray pulses affect the electronic structure.

To further investigate possible X-ray pulse-induced effects on the XES signal, two different X-ray pulse lengths, ~50 fs and ~100 fs, and excitation energies, 7 keV and 9.5 keV, were used to study their influence in the XES signal from $Mn_2^{III,IV}$Terpy. We did not observe any difference in the shape or the energy position of the Mn $K\beta_{1,3}$ spectra. Additionally, different fluences, obtained by attenuating the incident beam, were also used to compare the XES spectral shape. The Mn $K\beta_{1,3}$ spectra of $Mn_2^{III,IV}$Terpy collected using an incident flux of 10^{12} and 5×10^{10} photons per pulse at 7 keV and 50-fs pulse length were also identical.

Conclusion

We have shown that XES data from redox active transition metal complexes in aqueous solution can be collected at RT using the short femtosecond X-ray pulses at the LCLS. These results suggest that the XFEL-based probe-before-destroy method should also be applicable to other spectroscopic techniques such as X-ray absorption spectroscopy and resonant inelastic scattering spectroscopy in the hard X-ray energy range. This opens the door for time-resolved studies of the chemical dynamics of various catalytic systems and metalloproteins under functional conditions, by triggering reactions chemically, photochemically, or electrochemically.

It is important to note that the XES measurements can be performed in parallel with XRD measurements using the same photon energy for the incident X-ray pulses. For metalloproteins, redox active metal clusters play central roles in electron transfer and catalysis, and protein residues are often critical for mediating these reactions by providing pathways for electrons, protons, substrates, and products. To understand this intricate interplay between protein and metal cofactors, it is desirable to follow the chemical dynamics using spectroscopy simultaneously with the structural changes monitored by crystallography in a time-resolved manner under ambient conditions. $K\beta_{1,3}$ and $K\beta'$ lines provide intrinsic information about the electronic structure and the advancement of the catalytic intermediates. XES can also serve as an in situ method for monitoring the integrity of metal catalytic centers during XRD data collection; it has been shown in previous SR work (29–32) that an active site can already be fully damaged when the overall protein crystal structure is still intact.

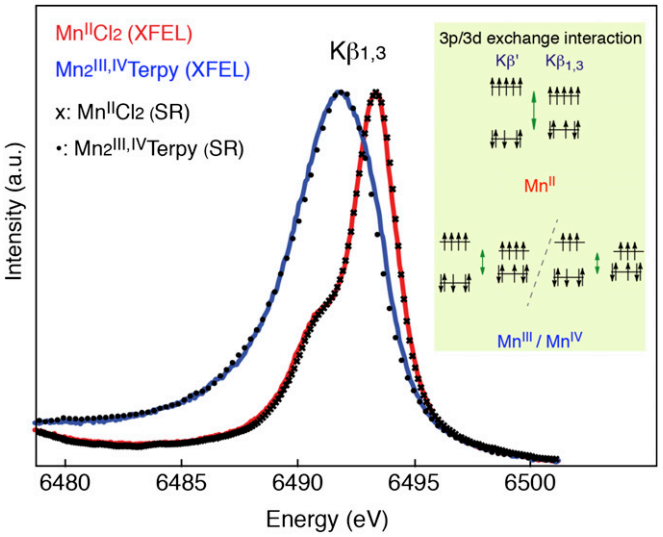

Fig. 3. The integrated $K\beta_{1,3}$ spectra from the Mn^{II} and $Mn_2^{III,IV}$ complexes. The integrated RT Mn $K\beta_{1,3}$ X-ray emission spectra of $Mn^{II}Cl_2$ (red, 500 mM Mn) and $Mn_2^{III,IV}$Terpy (blue, 180 mM Mn) were collected at the LCLS with 50-fs X-ray pulses. The symbols show $Mn^{II}Cl_2$ and $Mn_2^{III,IV}$Terpy spectra collected with a similar setup at a synchrotron for comparison purposes. The $K\beta_{1,3}$ spectrum arises from the 3d–3p exchange coupling (*Inset*) that makes the spectrum sensitive to the number of unpaired electrons in the 3d orbitals, thereby providing information about the spin state of the complex. For high-spin complexes the position of the peak, therefore, is an indicator of the oxidation state or charge density on the metal.

In principle, valence-to-core emission spectra ($K\beta_{2,5}$ and $K\beta''$ lines) can also be used for femtosecond XES studies, to collect ligand-sensitive information. However, they are about two orders of magnitude weaker in intensity (~200 times weaker for Mn) compared with the $K\beta_{1,3}$ and $K\beta'$ lines, making the experiments more challenging.

Materials and Methods

Experimental Conditions. The XES measurements were performed at the CXI instrument of the LCLS (43). The two inorganic Mn complexes, $Mn^{II}Cl_2$, 500 mM Mn, and $[Mn_2^{III,IV}O_2(2.2':6',2''$-terpyridine$)_2(H_2O)_2](NO_3)_3 \cdot 6H_2O$ (46) ($Mn_2^{III,IV}$Terpy), 180 mM Mn, were dissolved in a glycerol/water (3:7, wt/wt) mixture. The solution samples were injected into the X-ray probe in the CXI chamber by means of an electrohydrodynamic liquid jet (44) of several micrometers thickness at the interaction region using the cone-jet mode (47). X-ray pulses of ~50-fs and ~100-fs pulse length at a repetition rate of 120 Hz with an energy of 7 keV and 9.5 keV (bandwidth of ~80 eV) were used for excitation. The X-ray flux was ~10^{12} photons per pulse for ~50-fs pulses and 3×10^{11} photons per pulse for ~100-fs pulses, with a beam size diameter of 2 μm FWHM at the sample. The beam was attenuated using Si filters of different thicknesses.

Energy-Dispersive XES Spectrometer. A high-resolution, wavelength-dispersive X-ray emission spectrometer, based on the von Hamos geometry (48), consisting of a 4×4 array of analyzer crystals, was designed to collect spectra at XFELs (Fig. 1 *Lower*). The spectrometer was commissioned at synchrotron sources (Stanford Synchrotron Radiation Lightsource and Advanced Light Source) and details are described elsewhere (28). The spectrometer was installed close to the horizontal plane with a central angle of 81° with respect to the beam direction. The cylindrically bent analyzer crystals (500-mm radius) collect the emitted radiation and diffract the selected energies, in accordance with Bragg's law, onto a 2D detector (Fig. 1 *Upper*). The signal was focused by the spectrometer to be centered in the detector in the

nondispersive axis (horizontal). To collect Mn $K\beta_{1,3}$ emission spectra, the Bragg angle range was set from 85.8° to 83.4°, equivalent to an energy range from 6,474.6 to 6,499.4 eV (limited by the detector size) for the Si(440) reflection. This corresponds to a position of 49 and 98 mm from the sample horizontal plane for the center of the crystal array and the detector, respectively. We estimate the energy resolution to be ~0.5 eV, as it was determined from synchrotron radiation measurements using a larger beam. The two Mn complexes were also measured at synchrotron radiation sources. The $Mn^{II}Cl_2$ spectrum was collected with the same von Hamos spectrometer using a Pilatus 100 K detector at room temperature (Advanced Light Source beamline 5.0.2), and the $Mn_2^{III,IV}$Terpy spectrum was collected with a scanning spectrometer in a cryostat at 10 K using a Vortex detector (Stanford Synchrotron Radiation Lightsource beamline 6–2).

XES Data Analysis. All images were treated initially with a dark current (pedestal) subtraction and corrected for common mode offset followed by application of an experimentally determined gain map. Single-pixel histograms of the recorded pixel values were constructed over all images contributing to the spectrum. Gaussian curves were fitted to the zero and one photon peaks of the histograms, enabling fine-tuned dark and gain corrections to the histograms directly from the data such that the zero photon peak is centered at zero analog-to-digital units and the separation between the zero and one photon peaks is identical for all pixels. The total count for each pixel was obtained by summing the analog-to-digital units values above a threshold of two-thirds the separation between the zero and one photon peaks. The final 1D spectra were obtained by integrating the signal in the nondispersive direction.

ACKNOWLEDGMENTS. We thank Prof. K. V. Lakshmi (Rensslaer Polytechnic Institute) for providing the Mn2III,IVTerpy sample. We thank the Linac Coherent Light Source (LCLS), Stanford Synchrotron Radiation Lightsource (SSRL), and Advanced Light Source (ALS) staff for their support. We thank John Morse and Gunther Haller for development and support with the Cornell-SLAC Pixel Array Detector at the LCLS/SLAC (Stanford Linear Accelerator Center). This work was supported by the Director, Office of Science, Office of Basic Energy Sciences (OBES), Division of Chemical Sciences, Geosciences, and Biosciences (CSGB) of the Department of Energy (DOE) under Contract DE-AC02-05CH11231 for X-ray spectroscopy instrumentation (to J.Y. and V.K.Y.); Director, Office of Science under Contract DE-AC02-05CH11231 (to N.K.S.) for data processing methods; and National Institutes of Health Grant GM55302 (to V.K.Y) for Mn bioinorganic chemistry and spectroscopy. Support from the Alexander von Humboldt Foundation (J.K.), and the National Institute of General Medical Sciences (P41GM103393) and National Center for Research Resources (P41RR001209) (U.B.) are acknowledged. The injector work was supported by LCLS (M.J.B. and D.W.S.); the AMOS program, CSGB Division, OBES, DOE (M.J.B); and the SLAC Laboratory Directed Research and Development award (to M.J.B. and H.L.). Support by Vetenskapsrådet, K&A Wallenberg Foundation (Artificial Leaf Umeå), and Umeå University (Solar Fuels Umeå) is acknowledged (J.M.). Experiments were carried out at LCLS and SSRL, National User Facilities operated for DOE, OBES by Stanford University, and at the ALS supported by the Director, Office of Science, OBES, DOE under Contract DE-AC02-05CH11231.

1. Emma P, et al. (2010) First lasing and operation of an angstrom-wavelength free-electron laser. *Nat Photonics* 4:641–647.
2. Chapman HN, et al. (2011) Femtosecond X-ray protein nanocrystallography. *Nature* 470(7332):73–77.
3. Aquila A, et al. (2012) Time-resolved protein nanocrystallography using an X-ray free-electron laser. *Opt Express* 20(3):2706–2716.
4. Koopmann R, et al. (2012) In vivo protein crystallization opens new routes in structural biology. *Nat Methods* 9(3):259–262.
5. Kern J, et al. (2012) Room temperature femtosecond X-ray diffraction of photosystem II microcrystals. *Proc Natl Acad Sci USA* 109(25):9721–9726.
6. Boutet S, et al. (2012) High-resolution protein structure determination by serial femtosecond crystallography. *Science* 337(6092):362–364.
7. Yano J, Yachandra VK (2009) X-ray absorption spectroscopy. *Photosynth Res* 102(2-3): 241–254.
8. Bertagnolli H, Ertel TS (1994) X-ray absorption spectroscopy of amorphous solids, liquids, and catalytic and biochemical systems–Capabilities and limitations. *Angew Chem Int Ed Engl* 33(1):45–66.
9. Koningsberger DC, Prins R, eds (1988) *X-ray Absorption: Principles, Applications, Techniques of EXAFS, SEXAFS and XANES* (Wiley, New York).
10. Chen LX (2005) Probing transient molecular structures in photochemical processes using laser-initiated time-resolved X-ray absorption spectroscopy. *Annu Rev Phys Chem* 56:221–254.
11. Bressler C, Chergui M (2010) Molecular structural dynamics probed by ultrafast X-ray absorption spectroscopy. *Annu Rev Phys Chem* 61:263–282.
12. March AM, et al. (2011) Development of high-repetition-rate laser pump/x-ray probe methodologies for synchrotron facilities. *Rev Sci Instrum* 82(7):073110–073110-8.
13. Vanko G, et al. (2010) Picosecond time-resolved X-ray emission spectroscopy: Ultrafast spin-state determination in an iron complex. *Angew Chem Int Ed Engl* 49(34): 5910–5912.
14. Messinger J, et al. (2001) Absence of Mn-centered oxidation in the S(2) → S(3) transition: Implications for the mechanism of photosynthetic water oxidation. *J Am Chem Soc* 123(32):7804–7820.
15. Pushkar Y, et al. (2010) Direct detection of oxygen ligation to the Mn4Ca cluster of photosystem II by X-ray emission spectroscopy. *Angew Chem Int Ed Engl* 49(4): 800–803.
16. Lancaster KM, et al. (2011) X-ray emission spectroscopy evidences a central carbon in the nitrogenase iron-molybdenum cofactor. *Science* 334(6058):974–977.
17. Mori RA, et al. (2010) Sulfur-metal orbital hybridization in sulfur-bearing compounds studied by X-ray emission spectroscopy. *Inorg Chem* 49(14):6468–6473.
18. Eeckhout SG, et al. (2009) Cr local environment by valence-to-core X-ray emission spectroscopy. *J Anal At Spectrom* 24:215–223.
19. Mori RA, et al. (2009) Electronic structure of sulfur studied by X-ray absorption and emission spectroscopy. *Anal Chem* 81(15):6516–6525.
20. Smolentsev G, et al. (2009) X-ray emission spectroscopy to study ligand valence orbitals in Mn coordination complexes. *J Am Chem Soc* 131(36):13161–13167.
21. Beckwith MA, et al. (2011) Manganese Kβ X-ray emission spectroscopy as a probe of metal-ligand interactions. *Inorg Chem* 50(17):8397–8409.
22. Heijboer WM, et al. (2004) K beta-detected XANES of framework-substituted FeZSM-5 zeolites. *J. Phys. Chem. B* 108:10002–10011.
23. Glatzel P, Bergmann U (2005) High resolution 1s core hole X-ray spectroscopy in 3d transition metal complexes—Electronic and structural information. *Coord. Chem. Rev.* 249(1–2):65–95.
24. Bergmann U, et al. (1999) Chemical dependence of interatomic X-ray transition energies and intensities—A study of Mn K beta'' and K beta(2,5) spectra. *Chem Phys Lett* 302(1):119–124.
25. Bergmann U, Glatzel P (2009) X-ray emission spectroscopy. *Photosynth Res* 102(2–3): 255–266.
26. Bergmann U, Cramer SP (1998) A high-resolution large-acceptance analyzer for X-ray fluorescence and Raman spectroscopy. *Proc SPIE* 3448:198–209.
27. Kleymenov E, et al. (2011) Five-element Johann-type X-ray emission spectrometer with a single-photon-counting pixel detector. *Rev Sci Instrum* 82(6):065107–065113.
28. Alonso-Mori R, et al. (2012) A multi-crystal wavelength dispersive x-ray spectrometer. *Rev Sci Instrum* 83(7):073114–073119.
29. Yano J, et al. (2005) X-ray damage to the Mn4Ca complex in single crystals of photosystem II: A case study for metalloprotein crystallography. *Proc Natl Acad Sci USA* 102(34):12047–12052.
30. Corbett MC, et al. (2007) Photoreduction of the active site of the metalloprotein putidaredoxin by synchrotron radiation. *Acta Crystallogr D Biol Crystallogr* 63(Pt 9): 951–960.
31. Meharenna YT, Doukov T, Li H, Soltis SM, Poulos TL (2010) Crystallographic and single-crystal spectral analysis of the peroxidase ferryl intermediate. *Biochemistry* 49(14): 2984–2986.
32. Grabolle M, Haumann M, Müller C, Liebisch P, Dau H (2006) Rapid loss of structural motifs in the manganese complex of oxygenic photosynthesis by X-ray irradiation at 10–300 K. *J Biol Chem* 281(8):4580–4588.
33. Young L, et al. (2010) Femtosecond electronic response of atoms to ultra-intense X-rays. *Nature* 466(7302):56–61.
34. Fang L, et al. (2010) Double core-hole production in N_2: Beating the Auger clock. *Phys Rev Lett* 105(8):083005–083009.
35. Cryan JP, et al. (2010) Auger electron angular distribution of double core-hole states in the molecular reference frame. *Phys Rev Lett* 105(8):083004–083008.
36. Berrah N, et al. (2011) Double-core-hole spectroscopy for chemical analysis with an intense X-ray femtosecond laser. *Proc Natl Acad Sci USA* 108(41):16912–16915.
37. Kanter EP, et al. (2011) Unveiling and driving hidden resonances with high-fluence, high-intensity x-ray pulses. *Phys Rev Lett* 107(23):233001.
38. Doumy G, et al. (2011) Nonlinear atomic response to intense ultrashort X rays. *Phys Rev Lett* 106(8):083002–083005.
39. Rohringer N, et al. (2012) Atomic inner-shell X-ray laser at 1.46 nanometres pumped by an X-ray free-electron laser. *Nature* 481(7382):488–491.
40. Vinko SM, et al. (2012) Creation and diagnosis of a solid-density plasma with an X-ray free-electron laser. *Nature* 482(7383):59–62.
41. Neutze R, Wouts R, van der Spoel D, Weckert E, Hajdu J (2000) Potential for biomolecular imaging with femtosecond X-ray pulses. *Nature* 406(6797):752–757.
42. Barty A, et al. (2012) Self-terminating diffraction gates femtosecond X-ray nanocrystallography measurements. *Nat Photonics* 6:35–40.
43. Boutet S, Williams GJ (2010) The coherent X-ray imaging (CXI) instrument at the Linac Coherent Light Source (LCLS). *New J Phys* 12:035024–035048.
44. Sierra RG, et al. (2012) Nanoflow electrospinning serial femtosecond crystallography. *Acta Crystallogr D Biol Crystallogr* 10.1107/S0907444912038152.
45. Koerner LJ, et al. (2009) X-ray tests of a pixel array detector for coherent x-ray imaging at the Linac Coherent Light Source. *J Instrum* 4:03001–03007.
46. Collomb MN, Deronzier A, Richardot A, Pecaut J (1999) Synthesis and characterization of a new kind of Mn_2(III, IV)μ-oxo complex: $Mn_2O_2(terpy)_2(H_2O)_2(NO_3)_3\,6H_2O$, terpy = terpyridine. *New J Chem* 23:351–353.
47. Gañán-Calvo AM (1997) Cone-jet analytical extension of Taylor's electrostatic solution and the asymptotic universal scaling laws in electrospraying. *Phys Rev Lett* 79: 217–220.
48. von Hámos L (1932) Röntgenspektroskopie und Abbildung mittels gekrümmter Kristallreflektoren [X-ray spectroscopy and imaging using a curved crystal reflector]. *Naturwiss* 20(38):705–706.